

Design and Fabrication of 3D-Printed Lab-On-A-Chip Devices for Fiber-Based Optical Chromatography and Sorting

Ole Milark, Marc Buttkewitz, Emil Agócs, Beate Legutko, Benjamin Bergmann, Janina Bahnemann, Alexander Heisterkamp, and Maria Leilani Torres-Mapa*

Microfluidic lab-on-a-chip (LOC) devices have become essential tools for multitudes of applications in various research fields. 3D printing of microfluidic LOC devices offers many advantages over more traditional manufacturing processes, including rapid prototyping and single-step fabrication of complex 3D structures. In this work, 3D-printed microfluidic devices are designed and fabricated for optical chromatography and sorting. Optical chromatography is performed by inserting a single-mode optical fiber into the device creating a counter-propagating laser beam to the fluid flow. Particles are separated depending on refractive index and size. To demonstrate optical sorting, a cross-type sorter 3D-printed microfluidic device is fabricated that directs the laser beam perpendicular to the flow direction. Design features such as a sloping channel and a channel configuration for 3D hydrodynamic focusing (to aid in controlled sample flow and particle position) help to optimize sorting performance. Stable optofluidic trapping and sorting are successfully achieved using the fabricated microfluidic devices. These results highlight the tremendous potential of 3D printing of microfluidic LOC devices for applications aimed at the optofluidic manipulation of micron-sized particles.

1. Introduction


In recent years, significant progress has been achieved in the development of microfluidic components for a variety of applications in fields—ranging from medical diagnostics and pharmaceutical research to environmental monitoring and chemical analysis.^[1–4] As a result, lab-on-a-chip (LOC) devices have become increasingly flexible and versatile enabling entire laboratory processes to be functionally automated. However, the process of developing and producing microfluidics for LOC devices using conventional fabrication methods is both time- and labor-intensive, often spanning multiple days.^[5] Furthermore, whenever minor adjustments have to be made on the device, the whole process must be repeated. And for conventional techniques (such as soft lithography), fabrication of complex 3D structures inside the microfluidic devices

is also complicated to implement, requiring multiple steps during fabrication.^[6]

O. Milark, A. Heisterkamp, M. L. Torres-Mapa
Institute of Quantum Optics
Leibniz University Hannover
Welfengarten 1, 30167 Hannover, Germany
E-mail: torres@iqo.uni-hannover.de

O. Milark, A. Heisterkamp, M. L. Torres-Mapa
Lower Saxony Center for Biomedical Engineering
Implant Research and Development (NIFE)
Stadtfelddamm 34, 30625 Hannover, Germany

M. Buttkewitz
Institute of Technical Chemistry
Leibniz University Hannover
Callinstraße 5, 30167 Hannover, Germany

 The ORCID identification number(s) for the author(s) of this article can be found under <https://doi.org/10.1002/adpr.202400011>.

© 2024 The Author(s). Advanced Photonics Research published by Wiley-VCH GmbH. This is an open access article under the terms of the Creative Commons Attribution License, which permits use, distribution and reproduction in any medium, provided the original work is properly cited.

DOI: 10.1002/adpr.202400011

E. Agócs
Institute of High Frequency Technology
Technical University Braunschweig
38106 Braunschweig, Germany

E. Agócs, A. Heisterkamp, M. L. Torres-Mapa
Cluster of Excellence “PhoenixD” (Photonics, Optics and Engineering
Innovation Across Disciplines)
Hannover, Germany

B. Legutko, B. Bergmann
Institute of Production Engineering and Machine Tools
Leibniz University Hannover
An der Universität 2, 30823 Garbsen, Germany

B. Legutko, B. Bergmann, J. Bahnemann, A. Heisterkamp,
M. L. Torres-Mapa
SFB/TRR 298 “SIIRI” (Safety Integrated and Infection Reactive Implants)
Hannover, Germany

J. Bahnemann
Institute of Physics
University of Augsburg
Universitätsstraße 1, 86159 Augsburg, Germany

Advancements in 3D printing technology have revolutionized the precision and accessibility of microfluidic device production.^[5] 3D printing, also known as additive manufacturing, is a process of creating three-dimensional objects in a layer-by-layer accretive fashion based on a digital design. 3D printing of microfluidic structures allows for rapid and accurate fabrication of complicated microfluidic structures and offers a promising alternative to more conventional production methods. This technique also facilitates greater accessibility, requires less specialized knowledge, and enables the creation of more intricate 3D structures^[7] compared to existing methods. Although 3D printing allows for complete automation, one notable drawback is a considerable compromise in feature precision vis-à-vis the smallest printable channel width.^[8] A typical microfluidic channel size fabricated with soft lithography is only limited by diffraction, with 5 μm wide channels as standard. Fabrication of even smaller channels is possible with appropriate photomasks.^[6,9] In contrast, 3D-printed channel dimensions have typical channel dimensions over 100 μm ,^[6,10] although this has been demonstrated to be sufficient for many applications in biotechnology and optical manipulation.^[11–14]

While optofluidics is a well-established field, its integration into the realm of 3D-printed microfluidic devices is a relatively novel area that still holds considerable promise for investigation. Optofluidics enables label-free sorting and the trapping of colloidal particles and biological cells according to their refractive index and size. Specifically, microfluidic-driven optical chromatography works by using a weakly focused beam to impart optical force and oppose the viscous drag from the fluid flow.^[15] At a specific refractive index- and size-dependent distance from the beam waist, the drag force of the flowing medium and the optical scattering force of the laser beam acting on the particle reach an equilibrium point, the so-called retention distance.^[15] Optical chromatography has been used to passively sort samples of different sizes and similar particle sizes with different refractive indices.^[16,17] It was also used to separate spores of the same species but of different strains (i.e., *Bacillus thuringiensis* and *Bacillus athracis*).^[18] Precise size-selective sorting of metallic nanoparticles has been demonstrated using different laser wavelengths^[19] and phase gradient forces implemented in an optical line trap.^[20] In one recent study, for example, optical chromatography was reported in a flow-through configuration to sort between healthy and nutritionally deprived macrophages.^[21]

Crucial to the sorting performance of these systems is a stable fluid control maintained by the implemented microfluidic device. Conventional microfluidic systems with materials such as polydimethylsiloxane (PDMS)^[22] and plates of fused silica^[23] have been used for optical chromatography. Alternative approaches have utilized tapered glass capillaries^[24] and photonic crystal fibers^[25,26] as microfluidic channels to transport and confine colloidal particles,^[25] nanodiamonds,^[24] and propel

red blood cells,^[26] respectively, thereby increasing the laser-particle interaction range. A tapered fiber immersed in the nanoparticle containing solution was also implemented for sorting and transportation of nanoparticles.^[20,27] Although immersion of the fiber to the sample removes the need for microfluidic fabrication and simplifies the experiments, on-chip optical chromatography facilitates controlled fluid flow as well as contamination-free sample sorting and collection for further analysis.

By using 3D printing for microfluidic fabrication, iterative design and rapid prototyping can be performed to produce robust devices with optimal performance. Additionally, 3D printing does not require sophisticated laboratory facilities, which facilitates greater functional accessibility to optofluidic experiments in a low-cost research setting environment. Furthermore, 3D printing can strongly support reproducibility efforts. By openly sharing CAD designs or STL files among researchers, printing performance and fabricated devices can readily be compared across various commercially available 3D printers.

In this work, we report on facile 3D-printed microfluidic LOC for optofluidic experiments. We fabricated two microfluidic devices specifically designed for optical chromatography and sorting. In optical chromatography, particles are optofluidically trapped according to their retention distance, whereas in optical sorting, a cross-type configuration^[28] is used wherein particles are displaced by the optical force, while traversing through the laser beam acting perpendicular to the flow.^[21] Similar to optical chromatography, the particle displacement is dependent on the size and the refractive index of the particle. Colloidal samples with different sizes and refractive indices flowing through the laser beam can therefore be separated.^[15,22] The LOC device's capability to perform optical chromatography is demonstrated by comparing the experimental retention distances to theoretical values. Furthermore, the chip design for the cross-type sorter enables separation and collection of the sorted samples. In this work, we characterize the performance and limitations of the fabricated devices and seek to highlight the benefits of utilizing 3D printing as a fabrication technique for optofluidic LOC devices.

2. Experimental Section

2.1. Experimental Setup

The experimental setup used is shown in **Figure 1**. A solid-state Nd:YVO₄ laser (Solid State Laser, Smart Laser Systems, Berlin, Germany) emitted light at a wavelength of 1064 nm with a maximum power output of 3 W. The laser beam was demagnified using two lenses (L1 and L2), with L1 having a focal length of 75 mm and L2 having a focal length of 25 mm. The demagnified laser beam then passed through a half-wave plate (HWP) and a polarizing beamsplitter (PBS) to control the laser power. The HWP was mounted on a motorized rotation mount that was controlled with a custom-written LabVIEW program. The resulting beam was then directed into a single-mode (SM) fiber port (PAFA-X-4-C, Thorlabs, New Jersey, USA), which coupled the beam to a SM fiber (SM980-5.8-125-Custom-Muc, Thorlabs, New Jersey, USA) with a core diameter of 5.8 μm . The fiber delivered the laser beam with a maximum power of 950 mW into the fabricated microfluidic device.

J. Bahnemann
Centre for Advanced Analytics and Predictive Sciences (CAAPS)
University of Augsburg
Universitätsstraße 2, 86159 Augsburg, Germany

A. Heisterkamp, M. L. Torres-Mapa
Cluster of Excellence "Hearing4All"
Hannover, Germany

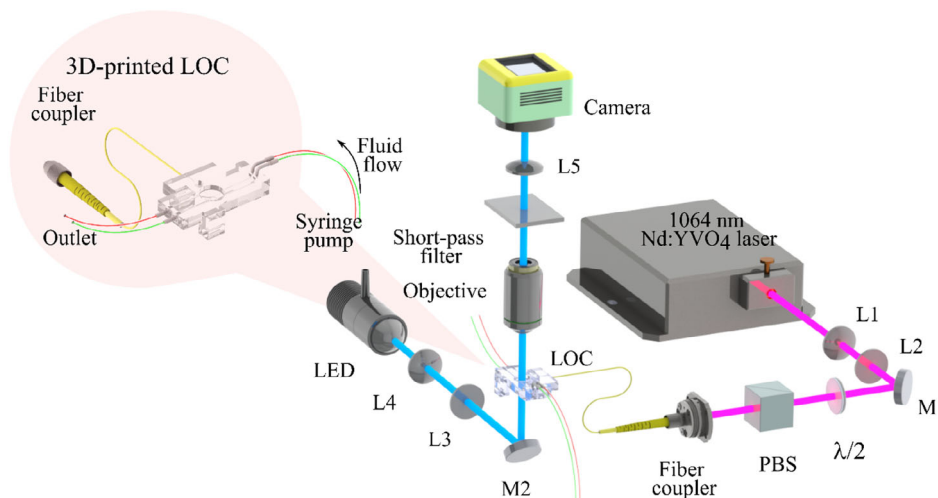


Figure 1. Experimental setup used for the optical chromatography and sorting experiments. This setup consists of multiple lenses (L1–L5) and multiple mirrors (M1 and M2). Before the laser enters the LOC device, the laser power is controlled by a half-wave plate (HWP) ($\lambda/2$) and a polarizing beamsplitter (PBS). The laser beam is coupled into a single-mode (SM) fiber through an SM fiber port (fiber coupler).

The LOC device was stably mounted onto a 3D-printed platform and then attached to a 3D XYZ stage with micrometer screws for position control in all directions. The setup included a microscope objective and a white LED light source. Köhler illumination was used to uniformly illuminate the LOC device with two lenses (L3 and L4). The focal length of L3 was 25.4 mm and the focal length of L4 was 50 mm. Depending on the magnification required, three different objectives were used: 1) a long working distance 50 \times objective (M Plan APO 50 \times , Mitutoyo, Kawasaki, Japan) with a NA of 0.55 and a working distance of 13 mm; 2) a 20 \times water dipping objective (XLUMPLFLN20XW, Evident, Tokyo, Japan) with a NA of 1.0 and a working distance of 2 mm; and 3) a 10 \times air objective (MPlanFLN, Evident, Tokyo, Japan) with a NA of 0.3 and a working distance of 11 mm. Lens L5 with focal length of 200 mm forms the image onto a CCD camera (340M-USB, Thorlabs, New Jersey, USA) with a pixel size of 7.4 μm and a maximum frame rate of 200.7 FPS. Placed between the microscope objective and the camera was a short-pass filter with a cutoff wavelength of 750 nm (FESH0750, Thorlabs, New Jersey, USA), which helped to ensure that no scattered laser light got captured by the camera.

Two syringe pumps were also used in these experiments: 1) a very precise programmable syringe with two syringe slots (Pump 11 Elite, Harvard Apparatus, Massachusetts, USA) featuring a minimum smooth flow of 1.28 pl min^{-1} and 2) a single syringe slot with a minimum flow of 1.67 nl min^{-1} (KDS 100 Legacy Syringe Pump, KD Scientific, Massachusetts, USA). Luer lock 3 mL syringes (Omnifix Luer Lock Solo, 4617022V, BBraun, Melsungen, Germany) were utilized and attached to tubes with an outer diameter of 1.6 mm and an inner diameter of 0.8 mm. These tubes were inserted into the LOC device and sealed using a custom 3D-printed clamp consisting of two parts. The assembly was then sealed using a rubber between the clamp and the LOC device. Both parts were fixed with an M4 screw and respective nut. The samples used in the experiments were spherical polystyrene (PPS-3.0, PPS-5.0, PPS-10.0, Kisker Biotech GmbH & Co. KG, Steinfurt, Germany), silica (PSI-3.0, PSI-5.0, PSI-10.0,

Kisker Biotech GmbH & Co. KG, Steinfurt, Germany), and melamine–formaldehyde co-polymer (MF-R-5.0, microParticles GmbH, Berlin, Germany) microparticles of different sizes diluted in deionized water. The ratios were set differently for every experiment.

2.2. LOC Device Fabrication

The LOC devices were designed using the computer-aided design software Inventor (Autodesk). All devices and prototypes were 3D-printed using a high-resolution 3D printer (AGILISTA-3200 W, Keyence, Neu-Isenburg, Germany) that is capable of achieving a printing layer thickness of 15 μm , according to manufacturer’s specification. The printing materials used were the transparent, AR-M2 and a water-soluble support material, AR-S1. The LOC devices were 3D-printed using settings “high resolution” and “glossy.” Additionally, different mounting platforms for the LOC devices and the devices for tube insertion into the LOC devices were also 3D-printed with the same printer. After printing, the printed part was removed from the printing platform and excess support material was removed in an ultrasonic bath. Depending on the channel size and length, cleaning time varied between 15 min and several hours. During long cleaning times, the temperature was carefully monitored to avoid damaging the printed material—high cleaning temperatures can potentially induce holes on the channel ceiling or cause other small structural defects. Afterward, the channels were flushed with water and 70% ethanol until they were completely clean.

The SM fiber was prepared simultaneously. Both the jacket and the coating of the fiber were removed with a fiber stripper. The fiber end was then cut with a fiber cleaver (UCL Swift, CL-03, Daejeon, Korea) and cleaned with 70% ethanol. In order to ensure a clean cut, the laser power emitted at the fiber end was measured with a power meter.

The optical fiber was then inserted into the LOC device to permit visual monitoring under a stereomicroscope. The fiber was

glued to the microfluidic system using a UV glue (NOA68, Thorlabs, New Jersey, USA) and then cured under a 365 nm lamp for 30 min. Finally, the device was mounted onto the platform and the fiber to the respective fiber port. Before and after each experiment, the LOC device was flushed multiple times with deionized water and 70% ethanol.

2.3. 3D-Printed Material Characterization

Transmission measurements were performed on rectangular 3D-printed samples (10×35 mm) with varying thicknesses between 200 and 1000 μm using a calibrated, unpolarized, light source with a wavelength range between 300 and 950 nm (Ocean Insight, HL-3P-INT-CAL, Orlando, Florida, USA) and a spectrometer (Ocean Insight, Flame-T-XXR1-ES, Orlando, Florida, USA). The transmission at 1064 nm was measured using the same laser for optical sorting experiments. The 3D-printed samples were irradiated with a collimated beam and the incident and transmitted laser power were measured with a power meter. Refractive index measurements were performed via ellipsometry. To eliminate the backside reflections during the measurements, three 1 mm 3D-printed thick samples were prepared and attached to a 10 mm thick glass plate using a refractive index matching oil. The samples were measured in the wavelength range between 350 nm and 1050 nm using an angle of incidence between 50° and 65° with 5° degree steps. The optical properties of the polymer were described using a Cauchy model with three

parameters. The extinction coefficient was not considered and was set to 0 in the model. To measure the surface roughness in the channel, we fabricated two circular 3D-printed samples stacked on top of each other with 15 mm diameter, separated with 1 mm posts at the edges. The samples replicated the fabrication method of the channels in the LOC devices, which were filled with support material during the 3D printing process. The support material was removed by immersing the samples overnight in water and subsequently in 70% ethanol. The surface roughness of the 3D-printed sample exposed to the support material was analyzed using an optical confocal measuring device (Confovis, DuoVario, Jena, Germany) with no additional surface polishing or treatment performed. A measuring field of 2.2×2.2 mm was selected using an objective lens with a $50\times$ magnification. The measurements were evaluated with the software μsoft analysis premium 8.2 (Digital Surf, France).

3. Results and Discussion

3.1. Optical Properties of the 3D-Printed Materials

The 3D printing material used to fabricate the LOC devices has not yet been characterized in the literature or by the manufacturer. Therefore, we report on the material's optical properties to support the design process of the optofluidic devices. **Figure 2** shows the characterization of the optical properties of the printing material. The refractive index of the material as a function of wavelength

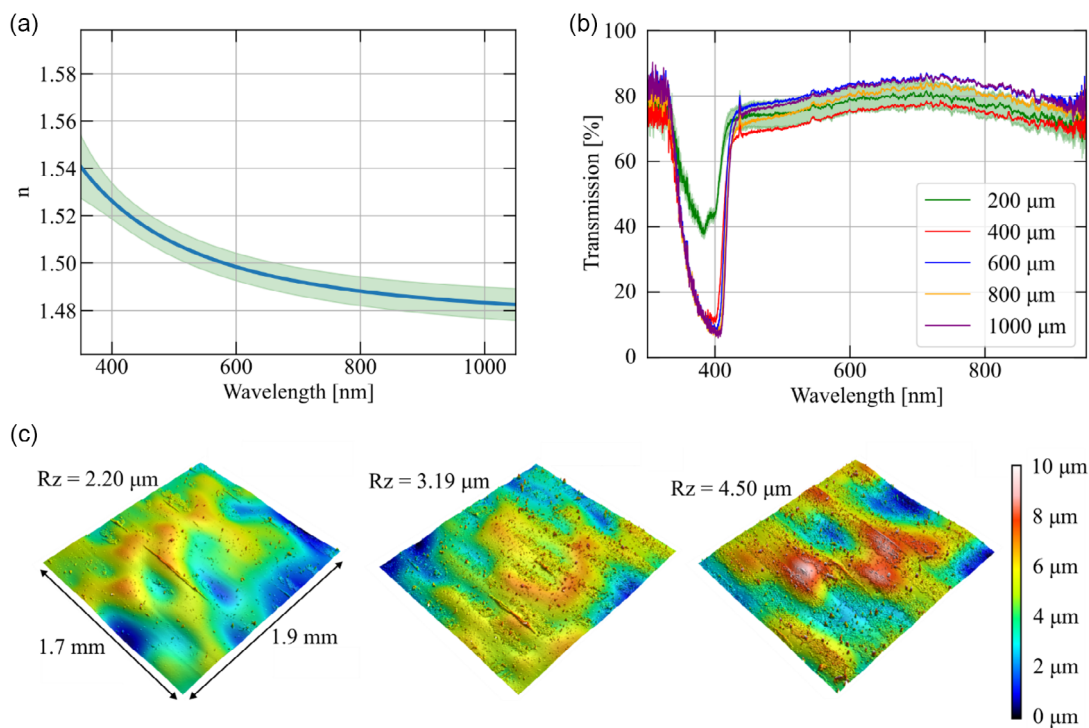


Figure 2. Optical properties of the transparent AR-M2 printing material. a) The refractive index, n , of the material in the wavelength range of 350–1050 nm. The shaded area is the standard deviation over six measurements, where three different 3D-printed samples were analyzed at two different spots. b) Transmission of the 3D-printed material with different thicknesses in the wavelength range of 300–950 nm. c) Surface topographies of three exemplary 3D-printed samples. The roughness parameter, R_z is used to characterize the height of the peaks of the surface topographies which states the average of the maximum height values of the evaluated regions.

measured in the range of 350–1050 nm is plotted in Figure 2a. In the visible range (400–700 nm), the refractive index is between 1.526 ± 0.008 and 1.492 ± 0.006 and monotonically decreases with longer wavelengths. Figure 2b depicts the transmission properties of the material for different wavelengths and different thicknesses. The transmittance is $\approx 80\%$ in the wavelengths between 430 and 950 nm and independent of the materials' thickness. Only 40% of light is transmitted through a sample thickness of 200 μm and reduces further to 10% with thicker samples in the wavelength range 330–430 nm. This wavelength range corresponds to the UV light source used to cure the 3D printing material. Figure 2c shows the surface topographies of three representative 3D-printed samples. The roughness parameter, R_z , provides the arithmetic mean of the maximum height values of the measurement segments with the surface profile filtered using a cutoff wavelength $\lambda_c = 0.8$ mm. This enables the separation of the roughness and the waviness of the surface. The surface topographies vary significantly from sample to sample with R_z values between ≈ 2 and 4 μm .

The optical properties such as refractive index, transmittance and absorbance properties as well as the surface roughness of the LOC device must be considered in designing optofluidic LOC devices. Especially for experiments requiring quantitative image acquisition or light delivery to the sample, the optical properties determine the quality of the images and the amount of delivered light to the sample. In our previous work, the LOC device printed using a different commercial 3D printer required a glass window for observation due to poor image quality acquired when imaging through the material.^[11] In contrast, the current 3D printing material (AR-M2) has sufficient light transmission at the visible range with micron-scale surface roughness. Hence, a glass window is not required which simplifies the fabrication process. The high transmittance measured at 1064 nm ($81.59 \pm 2.20\%$) using a collimated laser beam implies that optofluidic

experiments at this wavelength should not induce any significant damage to the device with minimal light scattering at the channel boundaries for wavelengths greater than 430 nm. However, the micron-scale roughness of the channels could affect the laser beam quality when the laser beam is transmitted through the material.

3.2. Design of an Optical Chromatography LOC Device

To demonstrate optical chromatography in a 3D-printed microfluidic system, a LOC device was designed and fabricated to implement the opposing optical and Stokes forces on micron-sized particles. The design of the microfluidic system includes a tubing integrated into the LOC device through a 3D-printed two-part mount, depicted in **Figure 3a**. A sealing ring was added between the two-part mount in order to ensure a tight seal when fastened using two M4 screws. As shown in the 3D CAD design of the device in Figure 3b, the LOC consists of a single-flow channel, with one input and one output on the same side. The channel has a width of 1 mm and a height of 400 μm (Figure 3c). To incorporate an optical fiber in the 3D-printed microfluidic system, a fiber channel was designed for fiber insertion. To avoid laser power loss as well as any aberrations in the beam profile due to the surface roughness of the channel, the fiber was inserted directly into the flow channel. The fiber channel was designed to have a width of 200 μm and a height of 200 μm at the narrowest portion positioned closest to the flow channel, which widens toward the outside of the microfluidic system for easier fiber insertion. On top of the fiber channel is a small well for UV glue used for fiber fixation into the LOC device and to seal the channel at the same time. Located above the region of interest is a pit with a height of 200 μm from the pit floor to the channel ceiling for microscopy. The pit thickness was sufficiently thin to acquire clear images but thick enough so that the device

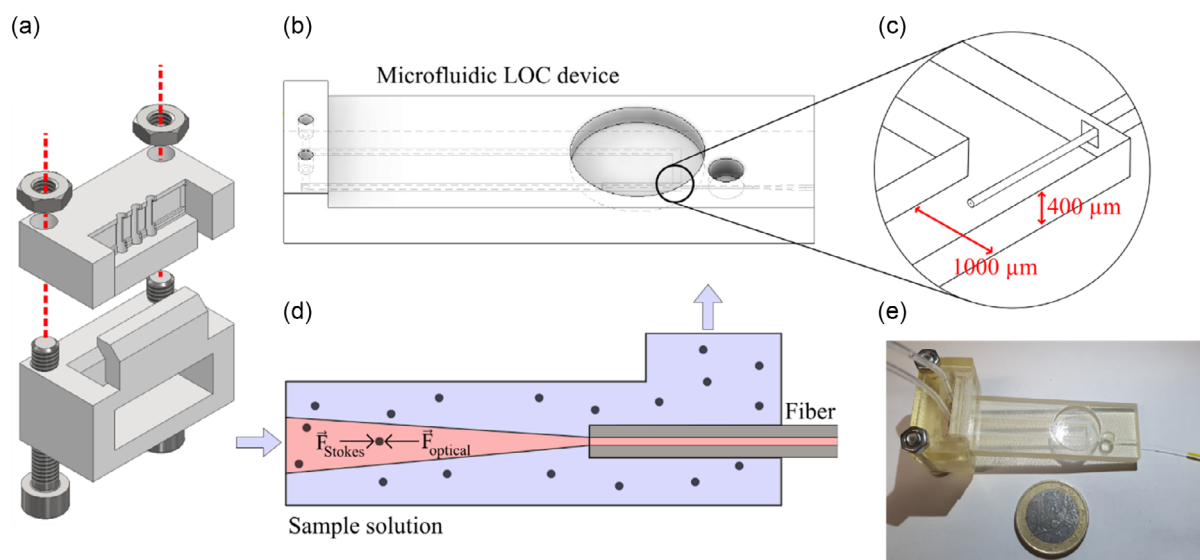


Figure 3. Illustrations of the microfluidic optical chromatography LOC device. a) The 3D-printed mount for tube insertion into the LOC device; an additional sealing piece was placed between both parts, in order to ensure that there is no leakage. b) The design as visualized with the CAD software. c) Exact dimensions of the channel with the inserted fiber. d) A visualization of the exact setup inside the channel, with the fluid flow direction from left to right. e) A photograph of the optical chromatography LOC device with an inserted tubing and an optical fiber—with the one-Euro coin included for scale.

remained sufficiently stable and robust for experimentation. The pit was used to accommodate the use of deionized water when water immersion objectives are used. Figure 3d shows the schematic diagram of the optical chromatography experiments. The fluid flow is directed from left to right in the opposite direction of the laser (which traverses the channel from right to left). A photograph of the completely assembled 3D-printed device, including the optical fiber and tubes inserted, can be seen in Figure 3e. The fabrication time of this LOC device was ≈ 3 h (i.e., 2 h for printing, 30 min for cleaning and 30 min for fiber insertion and curing), but we note that multiple LOC devices can actually be produced simultaneously without significantly extending the fabrication time.

3.3. Size and Refractive Index-Based Particle Separation in a 3D-Printed LOC Device

We performed optical chromatography with dielectric particles of different sizes and refractive indices using the fabricated 3D-printed LOC device. In order to perform optical chromatography, the microparticles flowing through the channel had to be affected by the laser beam in a manner where the drag force acted opposite to the optical scattering force. The fluid flow rate and

laser power were adjusted so that the optofluidically trapped particles were at a position observable under the microscope. By inserting the fiber directly in the sample channel, the laser beam retained its Gaussian intensity profile, which also permitted comparison of the retention distances with the theoretical predictions. Changes in fiber position due to variations in flow rate were not observed. During experiments, we ensured that only single particles were trapped at any given time in order to avoid light scattering when multiple particles are trapped simultaneously. Scattering due to multiple trapped particles can change the laser beam profile and alter the retention distance.

Retention distances of spherical particles were measured under varying flow speeds and laser powers. Polystyrene particles were suspended in deionized water at volume fractions of 1:500 for 10 μm , 1:1000 for 5 μm , and 1:4000 for 3 μm diameter particles. The distance between the fiber end and the particle was measured for each laser power, assuming that the beam waist is located at the fiber distal end. The flow speed of the sample was set to $v = 225 \mu\text{m s}^{-1}$ which was calculated using the continuity equation.

Figure 4a shows the measured retention distances for polystyrene particles of different particle sizes. Experiments were repeated for five different particles of each size and error bars represent combined measurement uncertainties and standard

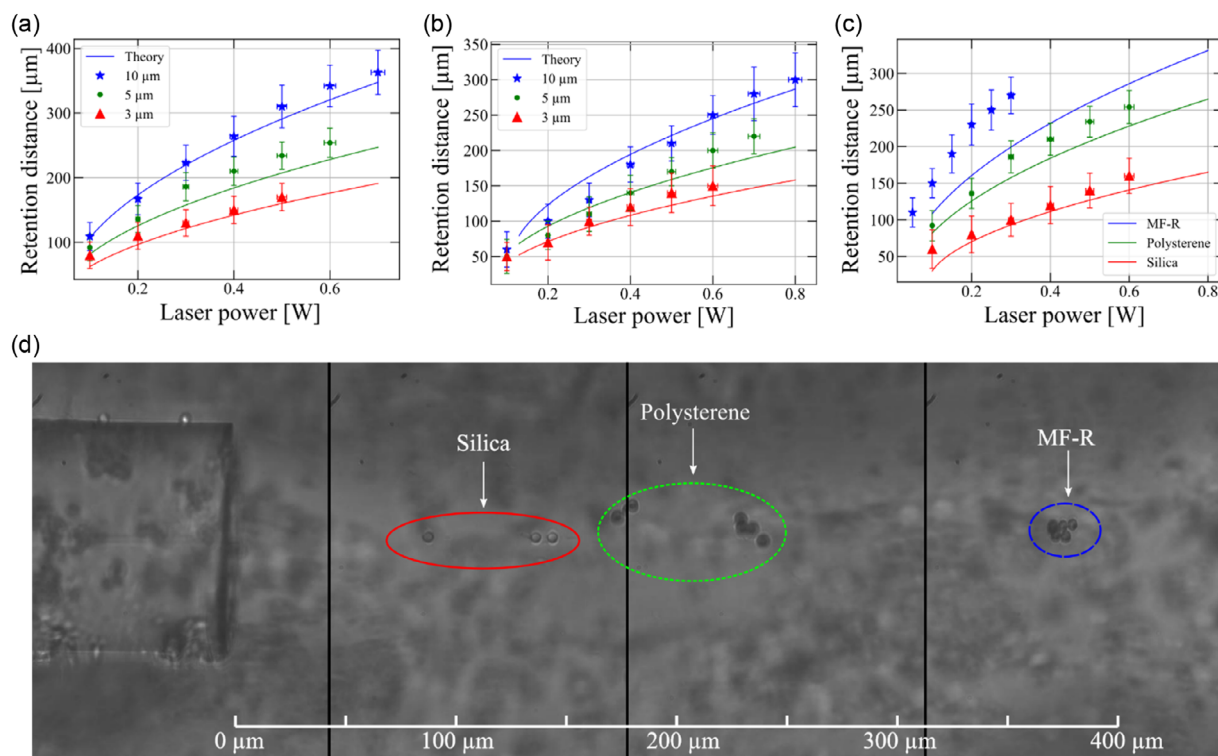


Figure 4. Optical chromatography in a 3D-printed LOC device. a) The plot shows the retention distances for different sized polystyrene particles at a flow speed of $225 \mu\text{m s}^{-1}$ for different laser powers. b) Graph shows the retention distance for different sized silica particles at a flow speed of $150 \mu\text{m s}^{-1}$ for different laser powers. c) Plot shows the retention distance for spherical polystyrene, silica and melamine/formaldehyde co-polymer (MF-R) particles with a diameter of 5 μm at a flow speed of $225 \mu\text{m s}^{-1}$ for different laser powers. d) Spliced image of optical chromatography performed in a 3D-printed microfluidic device. Silica, polystyrene and MF-R particles with particle diameter of 5 μm diameter show increasing retention distances. On the left side of the image is the fiber tip with the flow directed from right to left, set to $200 \mu\text{m s}^{-1}$. The laser beam with a power of 300 mW is scattered by the particles in the beam path, which leads to an uneven distribution of the particles. The image was created by merging multiple frames from a recorded video (Video S1, Supporting Information).

deviations. As expected, at a constant flow rate, the retention distance increased with increasing laser power due to the stronger scattering force by the laser beam. Furthermore, since the scattering force is proportional to the square of the particle radius, the retention distance also increased with increasing particle radius.

The retention distances were determined theoretically, by calculating the particle position at which the drag force (also called the Stokes force) and the optical scattering force reached equilibrium. At the retention distance, the Stokes force and optical scattering force can be described as:

$$F_{\text{Stokes}} = F_{\text{optical}} \quad (1)$$

where F_{Stokes} is the drag force of the fluid flow on the particle and F_{optical} is the optical scattering force of the laser beam.

The Stokes force is given by the relation:

$$F_{\text{Stokes}} = 6\pi\eta a v \quad (2)$$

where η is the dynamic viscosity of the surrounding medium, v is the flow speed and a is the particle radius.

The optical scattering force can be calculated using the following equation:

$$F_{\text{optical}} = \frac{2n_1 P}{c} \left(\frac{a}{\omega}\right)^2 \int_0^{\theta_{\text{max}}} \exp\left\{-2\left(\frac{a}{\omega}\right)^2 \sin^2(\theta)\right\} Q(\theta) \sin(2\theta) d\theta \quad (3)$$

where n_1 is the refractive index of the surrounding medium, P is the laser power, c is the speed of light in a vacuum, ω is the beam radius and θ is the incidence angle of the light on the particle.

The coefficient for the momentum transfer of the light onto the particle $Q(\theta)$ is defined as:

$$Q(\theta) = \frac{1}{2} \left[1 + R \cos(2\theta) - \frac{T^2 \{\cos(2\theta - 2\phi) + R \cos(2\theta)\}}{1 + R^2 + 2R \cos(2\phi)} \right] \quad (4)$$

where R and T are the Fresnel coefficients of reflection and transmission, respectively and ϕ is defined by Snell's law given by:

$$n_1 \sin(\theta) = n_2 \sin(\phi) \quad (5)$$

where n_2 is the refractive index of the particle.

Previous reports in optical chromatography assumed $a \ll \omega$ and a laser beam with a Gaussian intensity profile, which yields the standard formula for retention distance given by:

$$z = \frac{\pi \omega_0^2 n_1}{\lambda} \sqrt{\frac{n_1 P Q^* a}{3 \pi \eta \nu c \omega_0^2}} \quad (6)$$

where ω_0 is the beam waist of the laser beam, λ is the wavelength of the laser light and Q^* is the conversion coefficient of the momentum transfer from the light onto the particle.^[14] Q^* is the calculated integral from Equation (3), with the assumption that $a \ll \omega$. In our experiments, however, the assumption that $a \ll \omega$ is actually not applicable for all possible positions. Therefore, the optical scattering force was calculated using Equation (3) and the values of θ_{max} depend on the following condition:

$$\theta_{\text{max}} = \begin{cases} \tan^{-1}\left(\frac{\omega(z)}{a}\right) & \text{for } \omega(z) < a \\ \frac{\pi}{2} & \text{for } \omega(z) \geq a \end{cases} \quad (7)$$

The retention distances were then calculated by solving Equation (1) numerically. Solid lines in plots shown in Figure 4 show the retention distances predicted by this adapted formula. The measurements are in good agreement with the predicted values for the retention distance, with the retention distance of the 10 μm particles higher than the retention distances of the 5 and 3 μm particles, respectively. Figure 4b shows the results of a similar experiment conducted using silica particles. Compared to polystyrene ($\rho = 1.05 \text{ g cm}^{-3}$), silica has a significantly higher density ($\rho = 2.19\text{--}2.65 \text{ g cm}^{-3}$), which reduces the number of particles that reach the observation region. Accordingly, the concentration of silica particles in the sample was chosen to be higher than the concentration in the polystyrene samples. Silica particles were suspended in deionized water at volume fractions of 1:200 for 10 μm , 1:500 for 5 μm , and 1:500 for 3 μm sizes. For this measurement, we set $v = 150 \mu\text{m s}^{-1}$. Similar to the results of the polystyrene particles, the measured retention distances were found to be in good agreement with the theoretical predictions.

For short retention distances using a laser power of 100 mW and flow speed of $150 \mu\text{m s}^{-1}$, the Stokes force on silica particles would be higher than the maximum optical scattering force. In accordance with the theoretical retention distance, no optofluidic trapping should be possible. Nonetheless, optofluidic trapping was in fact observed, since the optical gradient force is strong enough at the beam waist to trap the particle, even though there is an absence of force equilibrium between Stokes and optical scattering force. Close to the fiber end, the optical gradient force also prevents particles from sinking outside the range of the laser beam. At farther distances from the beam waist, the optical gradient force weakens significantly. Therefore, the particles were observed to sink out of the laser beam at higher retention distances due to the stronger gravitational force than the optical gradient force acting on the particles. Since polystyrene has a lower density than silica, longer retention distances could be observed for the polystyrene particles. The maximum measurable retention distance for 10 μm polystyrene particles was $363 \pm 34 \mu\text{m}$, while the maximum distance measured for silica was $300 \pm 38 \mu\text{m}$.

To further confirm the capability of the 3D-printed microfluidic device to sort materials of different refractive indices, the retention distances of similarly sized 5 μm silica ($n = 1.45$ at 1064 nm),^[29] polystyrene ($n = 1.57$ at 1064 nm),^[30] and melamine/formaldehyde co-polymer (MF-R) ($n = 1.68$ at 589 nm)^[31] particles at the same flow speed were also measured. The influence of the refractive index to the retention distance is shown in Figure 4c. Silica, polystyrene, and MF-R particles were all suspended in deionized water at a volume fraction of 1:500, 1:1000, and 1:2000, respectively. All experiments were performed at $v = 225 \mu\text{m s}^{-1}$. MF-R particles exhibit the highest retention distances with $270 \pm 25 \mu\text{m}$ at a laser power of 300 mW, since their refractive index is the highest and therefore, experience the strongest scattering forces. While refractive indices for silica and polystyrene are readily available in literature for the laser wavelength used for the chromatography experiments, the refractive index for

MF-R particles was not available at 1064 nm. Therefore, the theoretical calculation of the retention distances for MF-R particles was performed using the MF-R refractive index at 589 nm. While this might partly explain the differences between the theoretical prediction and the measured retention values, the deviations are too substantial to be simply accounted by the discrepancy in refractive index at the wavelength it was measured. We assume then that light absorption could be a contributing factor to this discrepancy. Light absorption of the particles was unaccounted in the theoretical prediction, and absorption would lead to a repulsive force, hence a higher retention distance than predicted.

In order to visualize the separation of the different particles within the 3D-printed LOC device, a sample containing all three particle types combined with different volume fractions was used in the device. Polystyrene, silica, and MF-R particles were all present at a volume fraction of 1:2000, 1:500, and 1:2000, respectively, with a flow speed of $v = 200 \mu\text{m s}^{-1}$ and a laser power set to 300 mW. Figure 4d shows a composite image created by splicing together different images taken with a 20 \times objective, marking the different particle types and their respective retention distances (Video S1, Supporting Information). The broad particle position distribution for each particle type can be attributed to the multiple scattering events with multiple particles in the beam path, which was also observed in previous reports.^[15,22]

3.4. Design of an Optical Sorting LOC Device

To demonstrate the feasibility of optical sorting using a 3D-printed LOC device, a cross-type sorter configuration was

designed and implemented. **Figure 5a** shows the optical sorting LOC device used for the sorting experiments. **Figure 5b** illustrates the dimensions of the 3D focusing device and the sorting region. The schematic of the sorting process in this LOC device can be seen in **Figure 5c**. Larger particles will experience a stronger optical force and are therefore displaced further than the smaller particles. Particles were then sorted according to their size, subsequently exiting the device at two different outputs. A photograph of the device is shown in **Figure 5d**. The optical sorting LOC device has two inputs—one for the sheath fluid and one for the sample fluid. Additionally, the LOC device has dual outputs which can be used for sorting experiments. Instead of vertical outputs, the outputs of this device are designed horizontally in order to ensure that pressure differences in both output tubes were the same and therefore, that 50:50 splitting of the flow was possible. To minimize particle sedimentation before entering the sorting section of the device, the sample channel was designed to have a downward slope at an angle of 2.36°. The angle between the sheath and sample channel was set to 60° and the angle between the output channels was set to 90°. The channel has a width of 400 μm and a height of 600 μm at the sorting region. Fabrication time of this LOC device is ≈ 8.5 h for a single device (i.e., 2 h for printing, 8 h for cleaning and 30 min for fiber insertion and curing).

3.5. Simulations of Particle Behavior and Flow Velocity in Front of the Optical Fiber

Computational fluid dynamics simulations for particle and flow behavior in the LOC device were performed to verify the device's

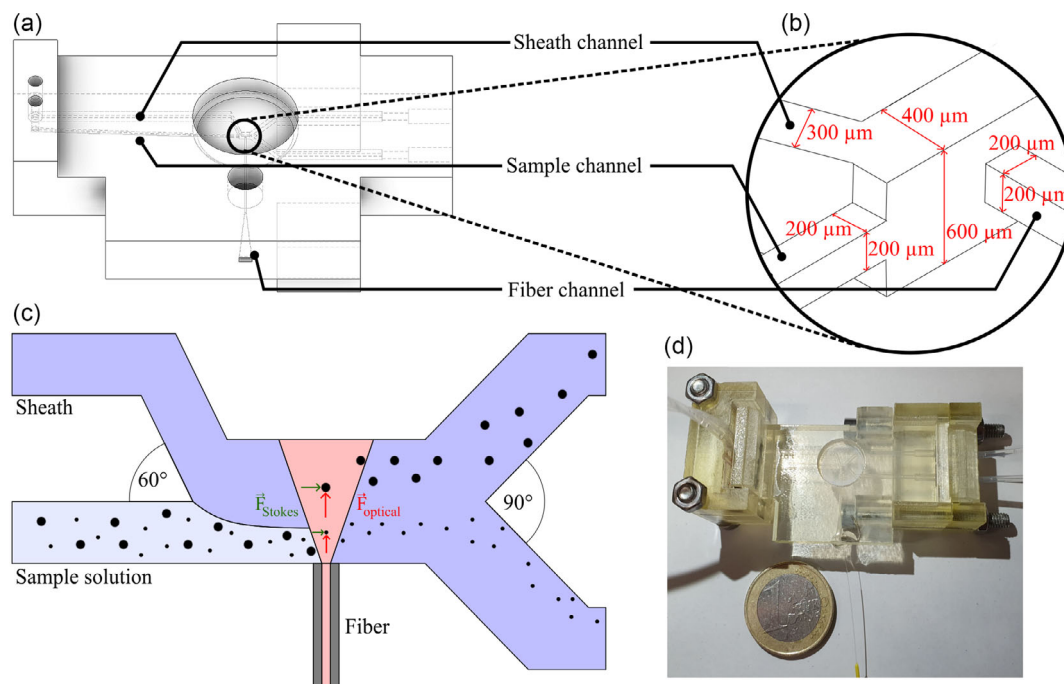


Figure 5. Illustrations of the fabricated microfluidic optical sorting LOC device. a) The device as seen in the CAD software. b) The exact dimensions of the 3D focusing part and the sorting region of the LOC device. c) A schematic of the optical sorting process inside the LOC device. In this case, the smaller particles exit the device at the bottom output, while the bigger particles exit through the top output. A force diagram depicting the Stokes force and the optical force is seen in the laser beam diameter. The optical force acts stronger on the bigger particle than on the smaller particle. d) A photograph of the optical sorting LOC device with inserted tubing and optical fiber. The one-Euro coin is included for scale.

ability to achieve 3D hydrodynamic flow focusing. The exact parameters and further relevant information regarding the simulations can be found in the Supporting Information. Flow rates for the sheath and the sample channel were chosen to be 0.2 and 0.1 mL h⁻¹, respectively, which are the same parameters that were used in the sorting experiments. The distribution and velocity of 10 μm polystyrene particles are shown in **Figure 6a**. In the absence of optical forces, the particles leave the sorting region through the bottom channel. Figure 6b shows the corresponding cross-sectional view of the particle distribution right in front of the fiber channel. Our simulations confirm the desired significant spatial confinement of the particles.

Further simulations were also performed to investigate the velocity and the concentration distribution and mimic the particle concentration in front of the fiber channel. Figure 6c shows the concentration distribution in front of the fiber, when the concentration inside the sample and sheath channel was 1 and 0 mol m⁻³, respectively. Both the particle and the concentration simulation showed similar velocity values in front of the fiber. 3D confinement of the sample fluid was observed, although it differed from the particle distribution profile due to the absence of diffusion in the particle simulation. The velocity distribution shown in Figure 6d depicts a typical Poiseuille flow profile directly in front of the fiber—with the velocity highest in the middle and decreasing radially toward the edges of the channel.

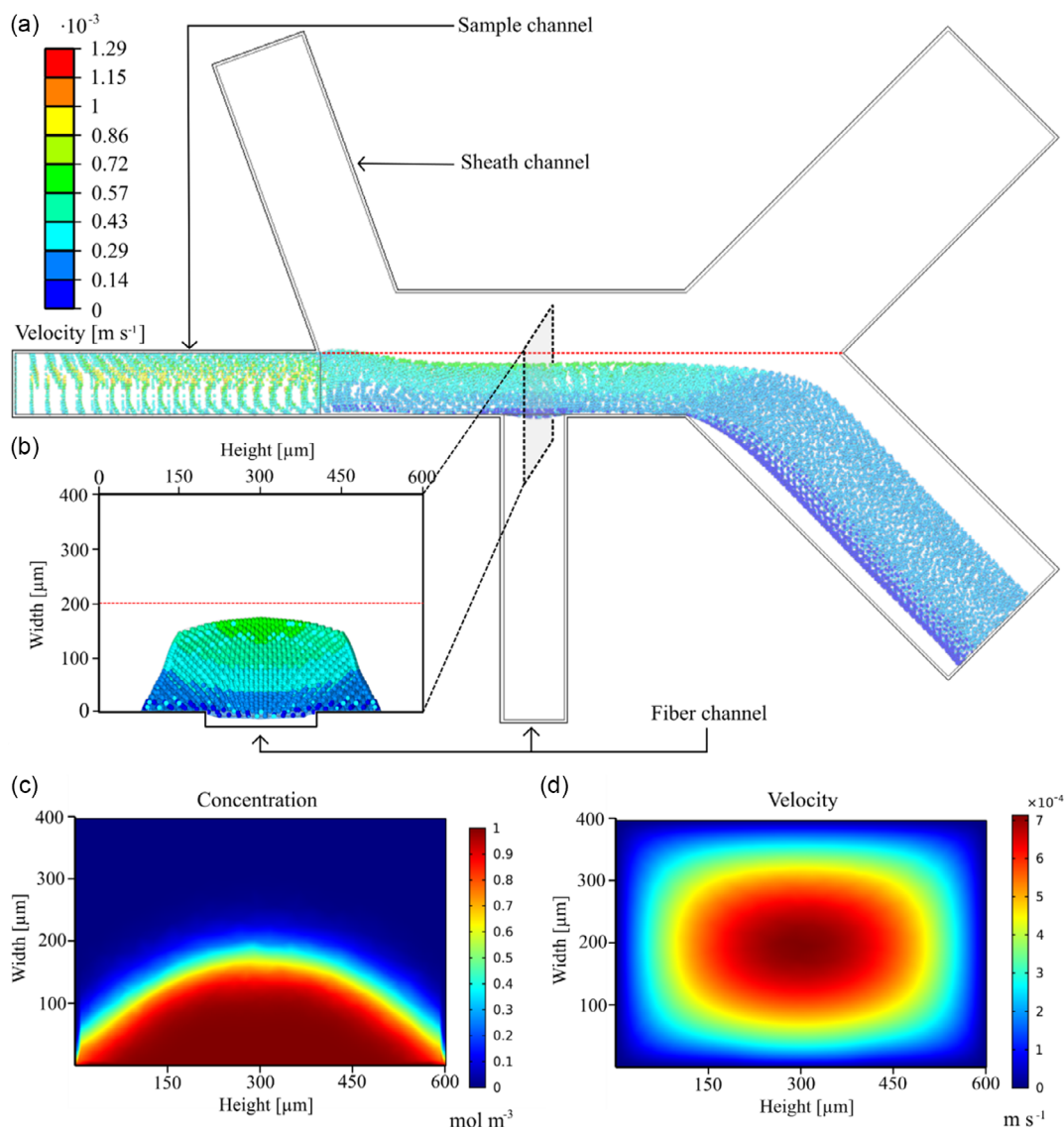


Figure 6. Simulations of particle and flow behavior inside the optical sorting LOC device. Flow rate was set to 0.2 mL h⁻¹ for the sheath fluid and 0.1 mL h⁻¹ for the sample fluid. a) The result of particle simulations without the optical force of the laser beam shows all particles exit the sorting region through the bottom channel. The red dotted line indicates the middle of the channel. b) The predicted particle distribution right in front of the fiber channel. Particles are 3D hydrodynamically focused by the sheath fluid. c) Plot of the concentration gradient right in front of the fiber channel. The sample concentration was set to 1 mol m⁻³, while the sheath concentration was set to 0 mol m⁻³. Once again, 3D hydrodynamic focusing can be observed. d) Flow velocity profile in front of the fiber channel.

As expected, the particle velocity highly depends on its position inside the channel.

3.6. Optical Sorting of Differently Sized Polystyrene Microparticles

An ideal sorting device should allow for both high sorting efficiency and reliable sorting consistency. Sorting efficiency refers to the proportion of correctly sorted particles in relation to the total particles processed in a sorting system. Particularly for optical sorting, a large number of particles have to traverse through the laser beam. To achieve high sorting consistency, particles with similar physical properties (such as refractive index and size) must be similarly affected by the laser beam. Accordingly, in an ideal scenario, all similarly sized polystyrene particles traversing the laser should be displaced at the same distance. A sorting device in which both these criteria are met would achieve a perfect on-chip sample sorting. Potential applications for such a microfluidic LOC sorter would include sample concentration,^[17] purification, fractionation^[23] and isolation of rare samples from a mixed sample population.^[32]

The designed optical sorting LOC device consists of a sample input and two outputs, and sorting experiments were performed using 5 and 10 μm polystyrene particles. Because the laser beam radius is significantly smaller compared to the channel size—due

to the limitations on the channel dimensions currently achievable via the 3D printer—the device was designed so that the particles could be further confined through the application of 3D hydrodynamic focusing. Even with such additional channel features, however, gravitational effects on the particles and flow rate constraints were observed to somewhat diminish sorting efficiency. Furthermore, the particles' varying entry positions into the laser beam led to displacement discrepancies. In short, while not every particle was perfectly sorted, collective sorting results nevertheless showed promise—leading to the conclusion that with the 3D-printed microfluidic LOC device, sorting can be achieved, albeit with somewhat limited efficiency.

Multiple experiments were conducted according to the sorting protocol (for details, see Supporting Information), to validate optical sorting using the optical sorting LOC device. Initial calibrations were performed to observe the particle positions of 5 and 10 μm polystyrene particles. For this, hydrodynamic focusing within the LOC device was analyzed to characterize the system. Polystyrene particles with a diameter of 5 μm were diluted in deionized water at a volume fraction of 1:250. Particle positions and average particle speed at the sorting region were then recorded using a camera and a 10 \times objective lens. As shown in the illustration in **Figure 7a**, due to hydrodynamic focusing, particles were focused and pushed toward the channel side where the fiber is situated. The farthest possible distance a

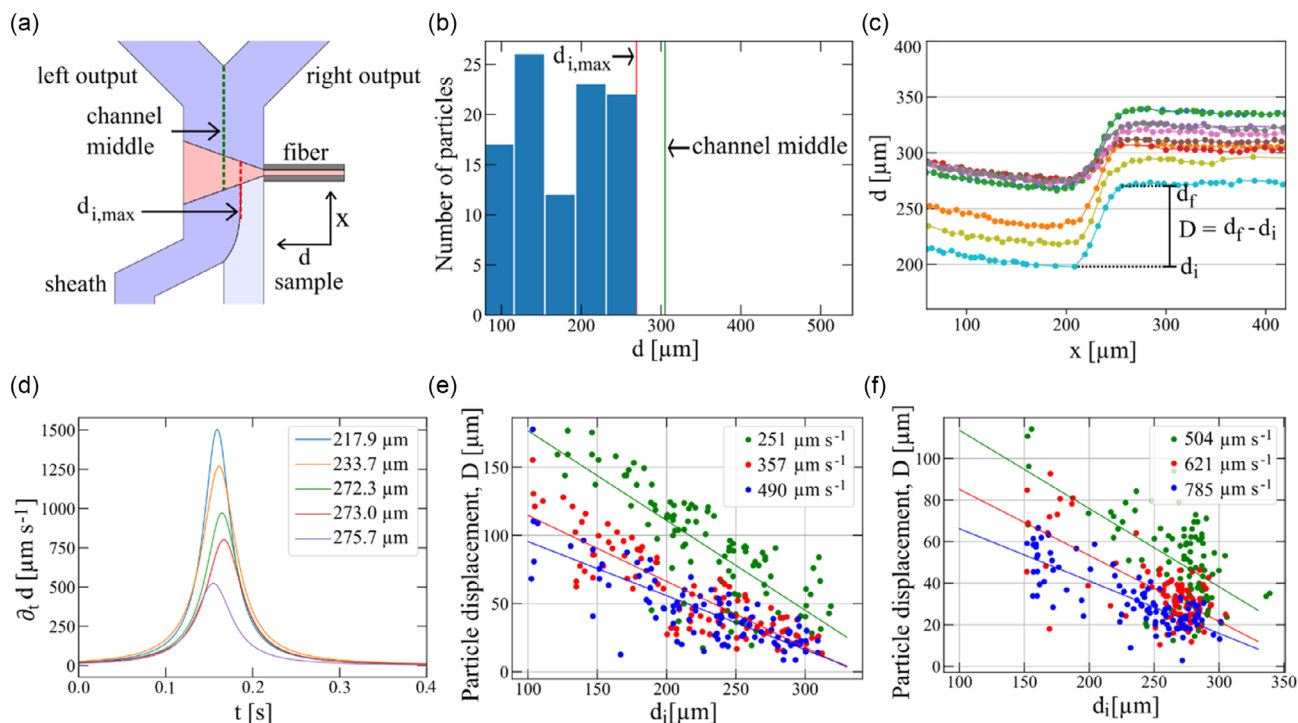


Figure 7. Calibration performed on the optical sorting LOC device. a) Sketch showing the optical sorting LOC device, where all important parameters are described and $d_{i,max}$ refers to the maximum possible initial position of the particles with respect to the laser beam. b) Plot shows the particle position in the channel of the optical sorting LOC device, with a sheath and sample flow rate of 0.2 and 0.1 mL h^{-1} , respectively. The distance to the fiber or the beam waist is abbreviated with d . c) Measured particle positions of 10 different 10 μm polystyrene particles traversing the laser beam. The definition of x can be seen in (a). At around $x = 210 \mu\text{m}$, the particles enter the laser and are displaced by the optical forces. d) Particle velocity for five different 10 μm polystyrene particles traversing the laser beam. The particles further from the fiber are slower than the particles closer to the fiber. Particle displacement (D) for e) 5 μm and f) 10 μm polystyrene particles depending on their initial distance (d_i) to the fiber end at a laser power of 950 mW. The graph includes three datasets, which correspond to different particle speeds. The data points were fitted using linear functions.

particle can be situated from the fiber tip is denoted by $d_{i,max}$. Measurements were performed under varying flow rates of sheath and sample flow. Figure 7b shows the particle distribution for a sheath flow rate of 0.2 mL h^{-1} and a sample flow rate of 0.1 mL h^{-1} . At the region of the channel close to the fiber side, the particles are distributed rather evenly. With a sheath flow rate of 0.2 mL h^{-1} and a sample flow rate of 0.1 mL h^{-1} , the minimum distance between the particles and the middle of the channel was measured to be $\approx 49 \mu\text{m}$. For sorting to occur, the $10 \mu\text{m}$ polystyrene particles should be displaced over the channel middle toward the left output, while the $5 \mu\text{m}$ particles must remain on the same side to exit the right output as illustrated in Figure 7a. Sorting under this condition is achievable, since both output channels have the same resistivity and therefore the same amount of fluid flows through both outputs.

Trajectory traces of 10 individual $10 \mu\text{m}$ polystyrene particles traversing through the laser beam can be seen in Figure 7c. Particle displacement (D) is defined as the difference from the initial position of the particle before it enters the laser beam (d_i) to its final position (d_f) or $|d_f - d_i|$. The corresponding velocity, $\partial_t d$ of $10 \mu\text{m}$ particles positioned at varying initial distances from the fiber tip (d_i) is shown in Figure 7d. Particles closer to the fiber have higher velocities than particles further away, since these particles experience a stronger optical scattering force. However, depending on the entry position of the particles with respect to the laser beam, their displacement can also vary as a result of the optical force. This is supported by the simulations, wherein the flow speed of the particles varies significantly depending on the position inside the channel. Since particles do not enter directly at the beam waist, the particle displacement could not be calculated theoretically. Therefore, the particle displacements have to be calibrated experimentally. We characterized the displacement of 10 and $5 \mu\text{m}$ polystyrene particles diluted in deionized water at a volume fraction of 1:100 and 1:250, respectively, with the laser power set to 950 mW . Particle positions were recorded both before and after moving through the laser beam. Linear functions were fitted to the measured values in order to approximate the particle behavior. Figure 7e,f show the calibration for 5 and $10 \mu\text{m}$ polystyrene particles, respectively. The plots depict the particle displacement as a function of the particle's initial position for varying particle speeds. For both particle sizes, faster particles experience shorter beam residence time, and correspondingly, smaller particle displacement. If we consider the scenario in an optical sorting device, where the 5 and $10 \mu\text{m}$ particles will be approximately traveling the same speeds, linear fits through 490 and $504 \mu\text{m s}^{-1}$ for 5 and $10 \mu\text{m}$, respectively, yield the following expressions, for $5 \mu\text{m}$: $D = 135 \mu\text{m} - 0.40 \cdot d_i$ and for $10 \mu\text{m}$: $D = 151 \mu\text{m} - 0.38 \cdot d_i$. The values of the slope of the linear fit are very similar; hence, the main difference between the two particles traveling at a similar speed could be derived from their y-intercept. The difference in their y-intercepts is $\approx 16 \mu\text{m}$, indicating that if 5 and $10 \mu\text{m}$ enter the laser beam with the same initial position and similar speed, the $10 \mu\text{m}$ particle would be displaced $16 \mu\text{m}$ farther than the $5 \mu\text{m}$ particle.

Notably, variations in particle displacements were observed, even though they enter the beam with the same flow speed and have the same distance from the beam waist. This could

be attributed to differences in particle height within the channel. Since the particle positions were only visualized from above, the respective height of the particles within the channel vis-à-vis the laser beam could not be determined and might foreseeably vary significantly from particle to particle. When entering the center of the laser beam, as opposed to the edges, particles experience the strongest scattering force. Additionally, since the channel size was significantly larger than the laser beam diameter (due to the 3D printing limitations noted earlier), only a small number of particles were actually propelled by the laser beam. For the reported characterization, only particles which were measurably displaced by the laser beam were considered.

Optical sorting was carried out with a sheath flow rate of 0.2 mL h^{-1} , a sample flow rate of 0.1 mL h^{-1} and laser power of 950 mW (Video S2, Supporting Information). The particle flow speed was measured to be around $490 \mu\text{m s}^{-1}$, on average. We expect that both with and without the laser, the right output would contain a similar proportion of 5 and $10 \mu\text{m}$ polystyrene particles. In contrast, under optical force, some $10 \mu\text{m}$ particles would be displaced and would exit the left output, thereby changing the proportion of particle composition collected in the left output.

Figure 8a,b show the percentage of total amount of each particle size collected at the left and right outputs without the laser, whereas Figure 8c,d illustrate the scenario when the laser is activated. We observed a change in the percentage of the number of particles collected from the left output when the laser was activated. In the absence of the laser beam, both the left and right output contained a similar fraction of 5 and $10 \mu\text{m}$ particles ($\approx 33\%$ of $5 \mu\text{m}$ and 67% of $10 \mu\text{m}$). By contrast, when the laser was present, the left output contained a higher percentage of $10 \mu\text{m}$ compared to $5 \mu\text{m}$ particles. Collected sample in the left output was composed of $18.40 \pm 3.68\%$ of $5 \mu\text{m}$ and $81.60 \pm 3.68\%$ of $10 \mu\text{m}$ polystyrene particles of the total counted particles. The right output contained $37.03 \pm 4.98\%$ of $5 \mu\text{m}$ and $62.97 \pm 4.98\%$ of $10 \mu\text{m}$ polystyrene particles—similar to the results observed without the laser. Our results therefore imply that the optical force displaced a proportion of the $10 \mu\text{m}$ particles over the middle of the channel, thereby effectively increasing the percentage of $10 \mu\text{m}$ particles in the left output.

We note that the reported sorting protocol was subject to certain limitations. Due to the low sorting efficiency, a significant number of particles remained unaffected by the laser beam and therefore exited the device through the right output. Additionally, at a certain step in the sorting process, the LOC device had to be flushed with an increased ($100\times$) flow rate in order to reduce particle sedimentation and increase the number of particles reaching the sorting area. During this step, all particles should have exited the device solely through the right output, even with the laser present, since the flow speed was too high for actual sorting to occur. Contrary to the simulation which shows that no particle should exit the left output, a few particles departed the sorting area through the left output, even without the laser (see Figure 8a). In this case, the total amount of particles at the left output were significantly lower compared to the right output (left output: 37 particles, right output: 723 particles, three separate experiments). This can be attributed to the changes in flow rate implemented during a single sorting experiment (see sorting protocol in the Supporting Information). During the

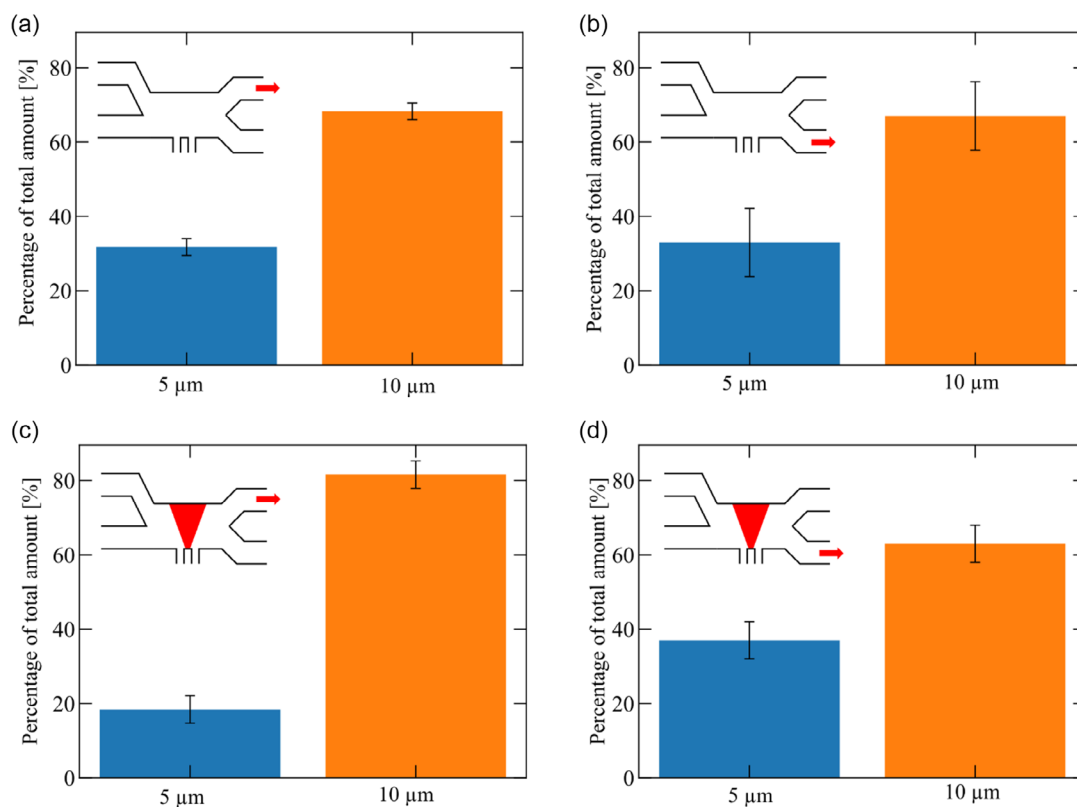


Figure 8. Optical sorting of 5 and 10 μm polystyrene particles. a,b) When the laser was off, both left and right output contained $\approx 32\%$ of 5 μm and 68% of 10 μm particles. c,d) When the laser was turned on, however, the right output remained approximately the same as with the laser off, while the left output was observed to contain 18.40% of 5 μm and 81.60% of 10 μm particles. Error bars are standard deviations from three independent measurements.

change of flow rate, unstable flow conditions could occur so that particles leave the sorting region through the left output. Despite this, the sorting efficiency remains valid, since this condition affects both the 5 and 10 μm by a similar proportion.

In both of the fabricated 3D-printed devices assessed in this work, the size of the channel dimensions of the 3D-printed LOC device was observed to constitute a substantial limiting factor in the sorting performance. Since the channel size was significantly bigger than the beam diameter (beam diameter was 5.8 μm at the beam waist, increasing to 70 μm at a distance of 400 μm), a significant number of particles were able to simply sink outside of the scope of the laser beam. Inside the optical chromatography LOC, this condition limited the maximum distance from the beam waist at which particles could be optofluidically trapped. By contrast, in devices created using traditional soft lithography methods, channel widths in the order of tens of micrometers can be achieved—thereby more effectively confining the particles and increasing laser–particle interaction, which naturally results in higher retention distances. Previous studies have reported higher retention distances for polystyrene and silica particles that utilize smaller channel widths at around 100–200 μm and lower flow speeds between 30 and 60 $\mu\text{m s}^{-1}$.^[15,16,22] In short, with smaller channels, samples containing a variety of multiple particle sizes can simply be sorted with greater efficiency. Nevertheless, in terms of the optofluidic sorting, we believe that by optimizing the flow rate and laser power, particles with size

differences in the order of nanometers (i.e., metallic or polymer nanoparticles and biological materials such as vesicles or extracellular exosomes) can still be sorted even within devices that feature larger channel diameters.

Overall, we demonstrate the successful design and fabrication of optofluidic LOC devices. Both optical chromatography and sorting were successfully implemented to separate colloidal particles based on their refractive index and size. Notwithstanding some practical constraints imposed by the present limitations of 3D printing technology, our work shows the tremendous potential of using 3D printing to fabricate LOC devices for optofluidic experiments. We envision combining 3D-printed microfluidics with low-cost and 3D-printed modular microscopy systems^[33,34] to enable wider dissemination both for scientific research and education purposes. To that end, the STL files of the fabricated devices, including attachments produced in this work can be found in the following link, <https://doi.org/10.5281/zenodo.11658470>. Previous studies have also shown that the 3D-printed devices fabricated using the same commercial 3D printer and 3D printing material are biocompatible and these 3D-platforms for mammalian cell culture do not lead to reduced mammalian cell viability.^[35,36] Therefore, the applications of such optofluidic 3D-printed microfluidic devices are not restricted to optofluidic chromatography and sorting of colloidal particles but can also be implemented for optical interrogation of samples containing bacteria or mammalian cells under continuous fluid flow.

4. Conclusion

In the present work, optical chromatography and optical sorting were implemented using 3D-printed microfluidic LOC devices. The optical chromatography LOC device was used for manipulation and separation of polystyrene, silica, and MF-R particles of different sizes. The measured results were in good agreement with the theoretical predictions derived from optical chromatography. The optical sorting LOC device was designed to be able to sort a sample containing differently sized microparticles. Within this device, a sample containing 10 and 5 μm particles was successfully separated based on their size differences. This work highlights the advantages of 3D printing for prototyping LOC devices—including the ability of this production mechanism to produce truly 3D channel features within a single fabrication step. This study also discusses some of the current limitations of this approach, however, including the need to rely on larger channel dimensions when compared to devices fabricated using other methods. Nevertheless, we show the great potential of 3D-printed devices for future applications in optofluidic research.

Supporting Information

Supporting Information is available from the Wiley Online Library or from the author.

Acknowledgements

The work was partially funded by the Deutsche Forschungsgemeinschaft (DFG, German Research Foundation) under the Collaborative Research Center SIIRI (SFB/TRR-298-SIIRI-Project ID 426335750) and under Germany's Excellence Strategy—PhoenixD (EXC 2122—Project ID 390833453) and Hearing4all (EXC 2177/1—Project ID 390895286). M.L.T.-M. acknowledges funding from Caroline Herschel Fellowship, Leibniz University Hannover. The authors thank Ammar Ahmed, Kristiana Topi and Christian Iriarte-Valdez for support in measurements. Open Access funding enabled and organized by Projekt DEAL.

Conflict of Interest

The authors declare no conflict of interest.

Data Availability Statement

The data that support the findings of this study are available from the corresponding author upon reasonable request.

Keywords

3D printing, lab-on-a-chip device, microfluidics, optical chromatography, optical sorting, optical tweezers, optofluidics

Received: January 19, 2024

Revised: June 16, 2024

Published online: August 1, 2024

- [1] Y. Yang, Y. Chen, H. Tang, N. Zong, X. Jiang, *Small Methods* **2020**, *4*, 1900451.
- [2] Y. Liu, L. Sun, H. Zhang, L. Shang, Y. Zhao, *Chem. Rev.* **2021**, *121*, 7468.
- [3] Z. Li, Y. Xu, W. Fang, L. Tong, L. Zhang, *Sensors* **2015**, *15*, 4890.
- [4] Y.-J. Wei, Y.-N. Zhao, X. Zhang, X. Wei, M.-L. Chen, X.-W. Chen, *Trends Anal. Chem.* **2023**, *158*, 116865.
- [5] C. M. B. Ho, S. H. Ng, K. H. H. Li, Y. J. Yoon, *Lab Chip* **2015**, *15*, 3627.
- [6] N. Bhattacharjee, A. Urrios, S. Kang, A. Folch, *Lab Chip* **2016**, *16*, 1720.
- [7] A. A. Yazdi, A. Popma, W. Wong, T. Nguyen, Y. Pan, J. Xu, *Microfluid. Nanofluid.* **2016**, *20*, 1.
- [8] A. K. Au, W. Lee, A. Folch, *Lab Chip* **2014**, *14*, 1294.
- [9] G. M. Whitesides, *Nature* **2006**, *442*, 368.
- [10] N. P. Macdonald, J. M. Cabot, P. Smejkal, R. M. Guijt, B. Paull, M. C. Breadmore, *Anal. Chem.* **2017**, *89*, 3858.
- [11] H. Wang, A. Enders, J.-A. Preuss, J. Bahnemann, A. Heisterkamp, M. L. Torres-Mapa, *Sci. Rep.* **2021**, *11*, 14584.
- [12] L. J. Frey, D. Vorländer, H. Ostsieker, D. Rasch, J.-L. Lohse, M. Breitedfeld, J.-H. Grosch, G. D. Wehinger, J. Bahnemann, R. Krull, *Sci. Rep.* **2021**, *11*, 7276.
- [13] T. Habib, C. Brämer, C. Heuer, J. Ebbecke, S. Beutel, J. Bahnemann, *Lab Chip* **2022**, *22*, 986.
- [14] J.-A. Preuss, G. N. Nguyen, V. Berk, J. Bahnemann, *Electrophoresis* **2021**, *42*, 305.
- [15] T. Kaneta, Y. Ishidzu, N. Mishima, T. Imasaka, *Anal. Chem.* **1997**, *69*, 2701.
- [16] S. J. Hart, A. V. Terray, *Appl. Phys. Lett.* **2003**, *83*, 5316.
- [17] S. J. Hart, A. Terray, J. Arnold, T. A. Leski, *Opt. Express* **2007**, *15*, 2724.
- [18] S. J. Hart, A. Terray, T. A. Leski, J. Arnold, R. Stroud, *Anal. Chem.* **2006**, *78*, 3221.
- [19] M. Ploschner, T. Čížmár, M. Mazilu, A. Di Falco, K. Dholakia, *Nano Lett.* **2012**, *12*, 1923.
- [20] F. Nan, Z. Yan, *Nano Lett.* **2018**, *18*, 4500.
- [21] Q. Lu, D. E. Barlow, D. Haridas, B. C. Giordano, H. D. Ladouceur, J. D. Gaston, G. E. Collins, A. V. Terray, *ACS Omega* **2019**, *4*, 12938.
- [22] P. C. Ashok, R. F. Marchington, P. Mthunzi, T. F. Krauss, K. Dholakia, *Opt. Express* **2010**, *18*, 6396.
- [23] A. Terray, J. D. Taylor, S. J. Hart, *Biomicrofluidics* **2009**, *3*, 044106.
- [24] C. Pin, R. Otsuka, K. Sasaki, *ACS Appl. Nano Mater.* **2020**, *3*, 4127.
- [25] M. K. Garbos, T. G. Euser, O. A. Schmidt, S. Unterkofler, P. S. J. Russell, *Opt. Lett.* **2011**, *36*, 2020.
- [26] S. Unterkofler, M. K. Garbos, T. G. Euser, P. S. J. Russell, *J. Biophotonics* **2013**, *6*, 743.
- [27] H. Fujiwara, K. Yamauchi, T. Wada, H. Ishihara, K. Sasaki, *Sci. Adv.* **2021**, *7*, eabd9551.
- [28] S. B. Kim, J. H. Kim, S. S. Kim, *Appl. Opt.* **2006**, *45*, 6919.
- [29] Y. Arosa, R. de la Fuente, *Opt. Lett.* **2020**, *45*, 4268.
- [30] X. Zhang, J. Qiu, J. Zhao, X. Li, L. Liu, *J. Quant. Spectrosc. Radiat. Transfer* **2020**, *252*, 107063.
- [31] H. Schnablegger, O. Glatter, *J. Colloid Interface Sci.* **1993**, *158*, 228.
- [32] X. Wang, S. Chen, M. Kong, Z. Wang, K. D. Costa, R. A. Li, D. Sun, *Lab Chip* **2011**, *11*, 3656.
- [33] B. Diederich, R. Lachmann, S. Carlstedt, B. Marsikova, H. Wang, X. Uwurukundo, A. S. Mosig, R. Heintzmann, *Nat. Commun.* **2020**, *11*, 5979.
- [34] Q. Meng, K. Harrington, J. Stirling, R. Bowman, *Opt. Express* **2020**, *28*, 4763.
- [35] I. G. Siller, A. Enders, P. Gellermann, S. Winkler, A. Lavrentieva, T. Scheper, J. Bahnemann, *Biomed. Mater.* **2020**, *15*, 055007.
- [36] I. G. Siller, N.-M. Epping, A. Lavrentieva, T. Scheper, J. Bahnemann, *Materials* **2020**, *13*, 4290.